EFFECTS OF DUST SCATTERING ON INTERSTELLAR JET LINE PROFILES

Nuria Calvet[1,2], Jorge Cantó[3], Luc Binette[4,1], and Alejandro C. Raga[5]

RESUMEN

El efecto de la dispersión por partículas de polvo en un medio estacionario alrededor de una fuente en movimiento, es el de ensanchar en velocidades el perfil gaussiano intrínseco de la fuente. La extensión en velocidad y la intensidad de las alas depende de las propiedades del polvo y de la profundidad óptica del medio. Los modelos teóricos pueden ser usados para estimar la inclinación del 'jet' con respecto a la línea de visión, la velocidad de la fuente y el espesor óptico hacia ella. En este trabajo se propone que las diferencias observadas entre los perfiles de las líneas de [S II] y Hα en los 'jets' asociados con HH 34 y HH 47 se deben a diferentes espesores ópticos hacia las regiones que emiten las líneas, lo cual se puede deber a que estas regiones tienen tamaños diferentes. Se discuten los efectos de la dispersión en la determinación del enrojecimiento que supone únicamente atenuación. Se encuentra que el espesor óptico determinado suponiendo únicamente atenuación, es menor que el espesor óptico verdadero de la región.

ABSTRACT

The effect of scattering by dust particles in a stationary medium surrounding a moving source is to spread in velocity the intrinsic gaussian profile of the source. The extent and strength of the wings depend on the dust properties and on the optical depth of the medium. Theoretical models can be used to estimate the inclination of the jet to the line of sight, the source velocity, and the optical depth towards the source. We propose that the differences between the [S II] and Hα line profiles in the jets associated with HH 34 and HH 47 are due to different optical depths to the line emitting regions, which could be due to different sizes for these regions. The effects of scattering in reddening determinations that assume only attenuation of the light of the source are discussed. It is found that the optical depth determined by assuming only attenuation is smaller than the actual optical depth of the region.

Key words: DUST – HERBIG-HARO OBJECTS – LINE PROFILE – RADIATION TRANSFER

I. INTRODUCTION

Faint filamentary structures in close association with Herbig-Haro objects and young stellar objects have been found in recent years in deep surveys in Hα and [S II]. These structures have typical projected length of 0.02 to 0.5 pc, a width to length ratio of 0.05 to 0.1, and a knotty morphology

1. Centro de Investigaciones de Astronomía, Venezuela.
2. Also Grup d'Astrofísica de la Societat Catalana de Fisica (Institut d'Estudis Catalans).
3. Instituto de Astronomía, UNAM, México.
4. Canadian Institute for Theoretical Astrophysics, Canada.
5. School of Mathematics, The University of Leeds, U.K.

(Mundt 1988, and references therein). This characteristic morphology and their line spectra, similar to that of HH objects and indicative of shock excitation with shock velocities of the order of 20 to 100 km s^{-1}, has lead most authors to interpret them as jets of supersonic material, ramming into the molecular clouds, and forming a series of internal shocks (Cantó, Raga, and Binette 1989, and references therein).

Low resolution spectroscopy of these jets indicate that the radial velocity of the emitting material with respect to the parent cloud is generally 50 to 100 km s^{-1}, while in some cases it can be as high as 400 km s^{-1}. Bührke, Mundt, and Ray (1988) have found [S II] $\lambda\lambda$ 6716, 6730 emission in the brightest parts of the jet associated with HH 34. The emission with a central peak and a structured wing extends up to 40 km s^{-1} from the central peak. The Hα

81

profile is quite different. It is broader and the peak is displaced by about 8 km s^{-1} with respect to the velocity of [S II] λ 6716. Furthermore, in the jet connecting HH 46 and HH 47, Meaburn and Dyson (1987) found a broad profile in Hα and for [SII], a structured wing extending $\sim$ 80 km s^{-1} from the main peak.

Meaburn and Dyson (1987) and Bührke *et al.* (1988) interpret the observed profiles in [S II] and Hα as arising from two components of different velocities. The high velocity component would originate from internal shocks, while the low velocity component would come from the boundary layer (Mundt 1988; see also Cantó and Raga 1991). The difference in the Hα profile is explained by having a much stronger low-velocity component in this line.

In this work, we present an alternative or complementary explanation in terms of dust scattering in the medium surrounding the emission region, which has proved to be important in determining the extended emission around HH objects (Noriega-Crespo, Calvet, and Böhm 1991) and the observed width of jets (Feldman and Raga 1991). Dust particles in the stationary environment receive and scatter photons emitted by the moving source; these photons are Doppler-shifted by an amount proportional to the velocity component of the source along the direction of the grain. Hence, the effect for an outside observer of the scattering by stationary dust particles surrounding a central moving source is to spread in velocity the intrinsic profile. The resultant line profile will be characterized by wings, whose strength and extent will depend on the properties of the dust particles and on the optical depth of the medium.

In order to estimate quantitatively this effect in a simple manner, we take a spherically symmetric homogeneous medium, located around a central source of finite size. We assume that photons are scattered only once. The single-scattering approximation becomes inappropriate when the optical depth of the medium becomes very large; to improve on this assumption, refined Monte-Carlo calculations must be performed. We feel that the exploratory nature of this work justifies our approximation. Great uncertainty is also found in the available data on grain properties that are needed to calculate line profiles, in particular, the albedo and the asymmetry factor. Although we refer mostly to the standard interstellar mixture, we also show some calculations using other grain sizes. In both cases, dust properties are very uncertain, so that the examples are mostly meant to give an idea of the variations of line profiles when varying the grain properties. When dust scattering is taken into account, we find that the observed extended wings can be reproduced with a single source emitting a gaussian line profile. We also find that differences in line profiles between lines of comparable wavelength can be explained in terms of differences in the optical depth in the respective line, which could be the result, for instance, of the different sizes of the emitting regions. For lines with sufficiently different wavelengths, the wavelength dependence of the extinction law and albedo will also result in differences in the profiles.

II. CALCULATIONS

a) *Radiative Transfer*

A spherically symmetric source is assumed to be immersed in a static homogeneous medium, moving relative to the medium with velocity v_s. The vector velocity v_s makes an angle θ with the line of sight. The size of the source is r_0, and it is emitting with an intensity $I_v^s = I_0 e^{-(v/v_0)^2}$, where v_0 is the intrinsic velocity width.

Photons from the source are reflected by the dust in the surrounding medium. Since the source is moving relative to the medium, dust grains will receive photons, which if scattered, will be Doppler-shifted by an amount corresponding to the component of the source velocity along the direction joining each grain and the source. Each scattered photon will have a probability, through the phase function, of being scattered towards the observer depending on the angle between the radius vector of the reflecting grain and the direction of the observer. In this work, we assume for simplicity that photons are scattered only once; this will not be a good approximation in the case of large optical depths. However, note that multiple scattering will not result in further Doppler-shifts (since the dust presents no velocity structure), but simply in a larger probability of escape (and therefore stronger wings).

We use two coordinate systems with the same origin at the source center. A system (x,y,z) with z in the direction of the observer, and a system (x',y',z') with z' in the direction of v_s. The systems are such that the angle θ corresponds to the rotation of system (x',y',z') relative to system (x,y,z) around axis $x = x'$. We solve the transfer equation for the specific intensity I_v at velocity v:

$$\frac{dI_v}{dz} = \eta_v - \chi I_v \ , \qquad (1)$$

along each ray specified by constant values of x and y. In this equation, η_v is the emissivity at velocity v and χ is the extinction (absorption plus scattering) at this velocity, which is constant over the line profile. The formal solution of the transfer equation is

$$I_v = \int_{-\infty}^{\infty} \eta_v e^{-\tau(z)} dz \; ; \qquad (2)$$

where the optical depth is given by

$$\tau(z) = \int_{-\infty}^{z} \chi dz \; , \qquad (3)$$

with the observer located at $z = -\infty$. For rays that intersect the source, a second term $I_v^s \, e^{-\tau}$ is added to the RHS of equation (2).

A grain located at $\mathbf{r}$ will receive an intensity from the central source given by

$$I_v^r(\mathbf{r}) = I_0 \, e^{-\tau_r(\mathbf{r})} \, e^{-[(v - \mathbf{v_s} \cdot \hat{\mathbf{r}})/v_0]^2} \; . \qquad (4)$$

Here, $\tau_r(\mathbf{r})$ refers to the optical depth in the radial direction between the source and the grain at radius $\mathbf{r}$. In the adopted coordinate system, $\mathbf{v_s} \cdot \hat{\mathbf{r}} = v_s z'/r$. The grain scattering emissivity is given by

$$\eta_v = \sigma_v \int \left(\frac{d\omega}{4\pi}\right) \Phi(\Theta) I_v^r(\mathbf{r}) \; ; \qquad (5)$$

where the integral is taken over the solid angle subtended by the source, $\pi(r_0/r)^2$. Here, Φ is the phase function, Θ the angle between the incident and reflected photon, which in the adopted system is given by $\cos^{-1}(z/r)$, and σ_v is the scattering coefficient. For simplicity, we assume that both $I_v^r(\mathbf{r})$ and Θ are constant over the source. We use the Henyey and Greenstein (1941) phase function,

$$\Phi = \frac{1 - g^2}{(1 + g^2 - 2g\cos\Theta)^{3/2}}, \qquad (6)$$

where g is the asymmetry factor.

We normalize all quantities, so I_v is measured in units of I_0, v is measured in units of v_0 and all distances are measured in units of r_0. The observed line flux at velocity v is given by

$$F_v = \int I_v d\omega = (r_0/d)^2 I_0 \int I_v dx dy \; , \qquad (7)$$

where d is the distance to the source. The total flux in the line is given by

$$F = (r_0/d)^2 I_0 v_0 \int dx dy \int I_v dv \; ; \qquad (8)$$

which can be expressed in terms of the total flux of the source alone

$$F^s = \pi^{3/2} (r_0/d)^2 I_0 v_0 \; , \qquad (9)$$

as

$$F = (F^s/\pi^{3/2}) \int dx dy \int I_v dv \; . \qquad (10)$$

b) Dust Properties

In this work, we find that line profiles are affected by the scattering of dust in the sense that the gaussian profile of the source develops "wings". The extent and strength of these wings will depend on the optical depth of the medium and on the assumed dust properties. The albedo $\bar{a}$ determines how much of the source light will be scattered by the dust, so that the stronger the albedo the stronger the wings become. The detailed shape of the profile, on the other hand, will depend on the asymmetry factor g (see below).

Lillie and Witt (1976) solved the radiative transfer problem in the Galaxy and determined the values of the albedo and the asymmetry factor that could reproduce the measurements of the galactic diffuse radiation obtained with the OAO 2 satellite at wavelengths between 1550 and 4250 A. Morgan, Nandy, and Thompson (1976) derived the value of the albedo at wavelengths 2350 and 2740 A fitting a theoretical model to the observations of the diffuse galactic background light obtained by the TD-1 satellite. These values were consistent within the errors with those determined by Lillie and Witt. Also, the values of $\bar{a}$ and g in the range between 3000 and 18000 A quoted by Mathis (1983) based on the model of Mathis, Rumpl, and Nordsieck (1977), agree reasonably well with the values of Lillie and Witt in the wavelength range where they overlap. In all cases, the value of the albedo is between 0.2 and 0.7, and the value of the asymmetry factor is between 0.2 and 0.8, in the range between 3000 and 10000 A. Although these values have large uncertainties, they are partially based on observations and we have used them in this work. For standard interstellar mixture (SIM), we adopt the values of the albedo and the asymmetry parameter as a function of λ from the compilation of Bruzual, Magris, and Calvet (1988), which is based on the authors quoted above. To obtain an extinction coefficient as a function of the gas density, we have used the tabulation of grain properties of Draine (1987), assuming a distribution of grain sizes proportional to $a^{-3.5}$, as suggested by the model of Mathis et al. (1977) and Draine and Lee (1984).

Since the profiles depend strongly on the dust properties, we also present profiles calculated for large grain sizes which have larger values of $\bar{a}$ and g than the standard interstellar mixture; these grains can produce wings that resemble more closely some of the observations. In this case, the grain properties at a given grain size are taken from Draine (1987).

III. RESULTS

Each model is characterized by a uniform density n_h, a source radius r_0 and a maximum radius r_{max}. The optical depth to the source is given by integrating equation (3),

$$\tau_\lambda = \chi_\lambda n_h r_0 \left(r_{max}/r_0 - 1 \right), \qquad (11)$$

where χ_λ is the dust extinction, considered constant along the line profile. We find that the resultant profiles depend, for fixed dust properties and as long as $r_{max} \gg r_0$, only on the optical depth at the given wavelength, that is, they depend on the individual characteristics of the region only through the combination given in equation (11). This is a fortunate result because it reduces the number of unknowns to only one, if the grain properties are known, namely, the optical depth at some reference wavelength.

a) *Line Profiles*

The emergent line profiles are similar to the source line profile, attenuated by the intervening optical depth, although they present more extended wings produced by dust scattering. To understand the process of formation of the scattered wings, consider the example shown in Figure 1. Around the axis z', defined by the direction of the source velocity v_s, we find cones of constant velocity v, defined by the condition $\cos\theta' = v/v_s = $ constant, where θ' is the opening angle of the cone. On this cone lay all the dust particles that receive photons from the source which will be Doppler-shifted by an amount $v_s\cos\theta'/c$. Figure 1 shows the projections of these cones on the plane $x = 0$, for viewing angles $\theta = 0°$, $45°$, and $90°$. The observer is in the direction of axis z, and the axis y is perpendicular to z in the plane of the figure, increasing to the right. For $\theta = 0°$, the cones are symmetric around the common axis $z = z'$. Dust located in the region $z \geq 0$, will Doppler-shift the scattered photons to $-v_s \leq v \leq 0$, while dust located in the region $z \leq 0$, will shift them to $0 \leq v \leq +v_s$. For $\theta = 90°$, dust located in the region $y \leq 0$, will Doppler-shift the scattered photons to $-v_s \leq v \leq 0$, while dust located in the region $y \geq 0$, will shift them to $0 \leq v \leq +v_s$. For intermediate angles, dust located in the hemisphere

defined by the condition $z' \geq 0$, will Doppler-shift the scattered photons to $-v_s \leq v \leq 0$, while dust located in the hemisphere $z' \leq 0$, will shift them to $0 \leq v \leq +v_s$. The physical regions emitting the scattered photons are clearly separated in the velocity domain. The order of the regions would be reversed if the source was receding from the observer, rather than approaching it.

The wings of the emergent line would not generally be expected to be symmetrical around the line center. On the one hand, the wings generated by dust scattering cover a range of velocities from $-v_s$ to $+v_s$, while the intrinsic profile of the source is centered at $v_s\cos\theta$. On the other, the amount of energy scattered at each velocity depends on the phase function of the grains and also on the extinction to the scattering grain within the region, as described below.

Dust particles located at the same distance r from the source will receive radiation attenuated by the same radial optical depth. The rate at which they will re-emit this radiation in the direction of the observer will depend on the phase function, which in turn, will depend on the angle Θ and the asymmetry factor g. If scattering is isotropic, $g = 0$, then photons are scattered in the direction of the observer at the same rate by all dust particles. On the other hand, if g tends to 1, then dust located between the source and the observer, close to the axis z, where $\Theta \sim 0$ will scatter photons at the highest rate. Figure 2 shows the comparison of profiles calculated with $\tau \sim 1$ and $\bar{a} \sim 0.6$ for $g = 0.002$ and $g = 0.8$, for the case $v_s/v_0 = -20$ and $\theta = 0°$ and $90°$. In the case of isotropic scattering dust scatters photons at an even rate at all velocities, while in the case of large g dust scatters more photons with $v \sim -v_s$, for $\theta = 0°$, and with $v \sim 0$, for $\theta = 90°$, and less photons with $v \sim 0$, for $\theta = 0°$, and with $v \sim \pm v_s$, for $\theta = 90°$, than in the isotropic case. The resultant line profiles are significantly different, as shown in Figure 2.

The extinction of the different scattering regions also affects the energy emerging at each velocity, because of the spatial distribution of the emission. For instance, for $\theta = 0°$, photons scattered at positive velocity are more extinguished than photons scattered at negative velocities (see Figure 1). For $\theta = 90°$, on the other hand, the energy scattered at $\pm v$ is attenuated similarly if the medium is uniform, and wings are expected to be symmetrical. At intermediate angles in between, we expect different emission throughput at $\pm v$, since photons scattered by dust along the cones of constant velocity at $\pm v$, travel different path lengths through the cloud and are extinguished in different amounts. For example, for $\theta = 45°$ in Figure 1, photons at a given $-v$ come from the region above the line marked $v = 0$ in the figure, while photons at the corresponding
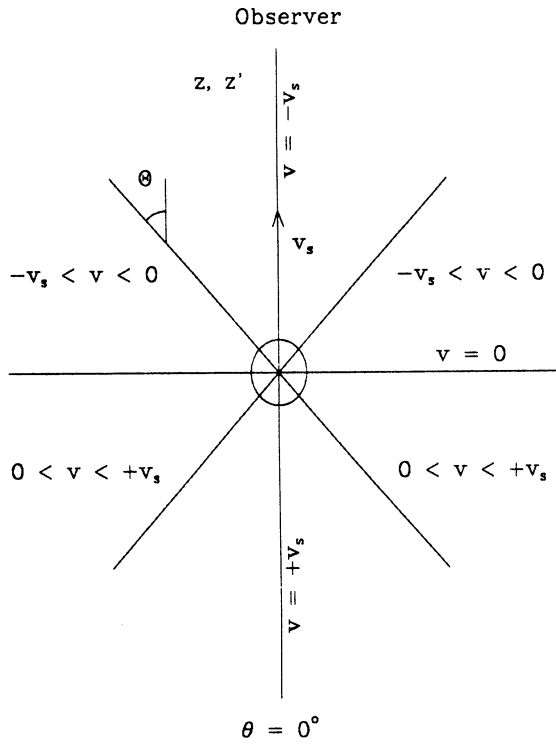
Fig. 1a. Positions of the constant radial velocity lines for different directions of the source velocity vector in the plane x = 0. The inclination to the line of sight, θ = 0°; the scattering angle, Θ, is indicated.
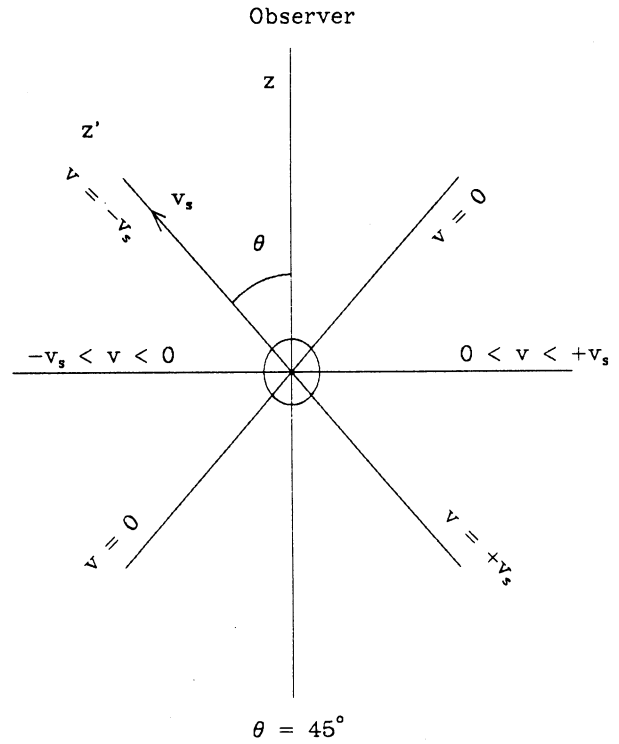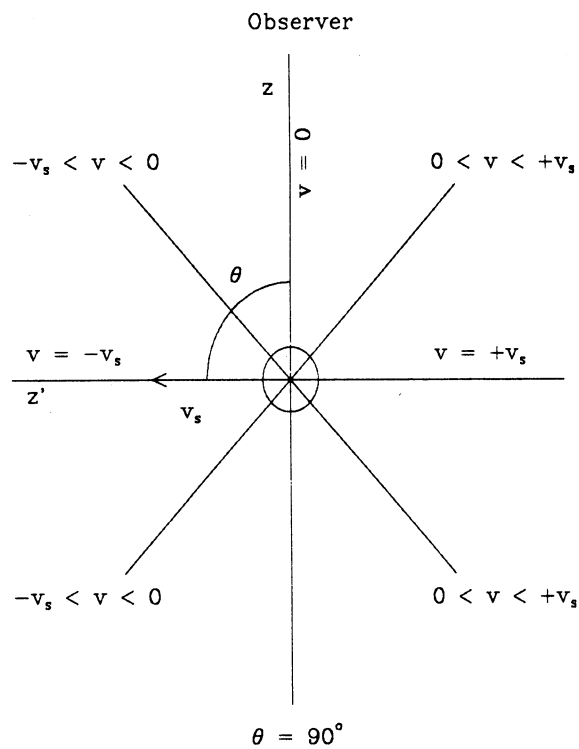
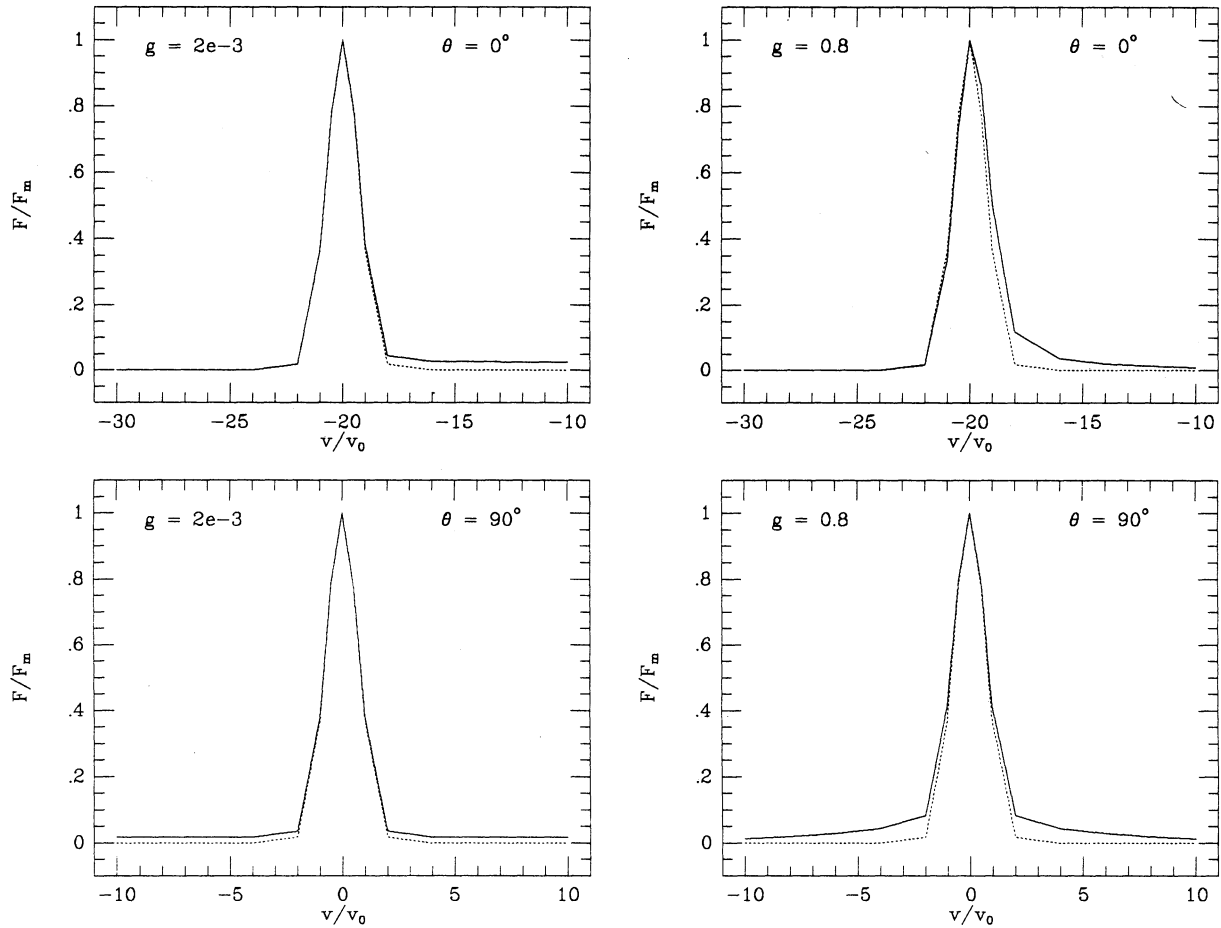Fig. 1b. Same as Figure 1a for θ = 45°.

Fig. 1c. Same as Figure 1a for θ = 90°.

Fig. 2. Comparison of profiles calculated for $g = 0.002$ and for $g = 0.8$. In both cases, $\tau \approx 1$, $\bar{a} \approx 0.6$. $v_s/v_0 = -20$.

velocity $+v$ come from the region below this line, and are overall more attenuated than those emerging at $-v$. The flux due to dust emission is therefore not symmetrical in the range $-v_s$ to $+v_s$, and the asymmetry might be more pronounced if the medium is not uniform.

Figure 3 shows line profiles calculated for: (a) the standard interstellar mixture, and (b) a grain size of $a = 0.2$ μm, for $\tau_V = 1$, 5, and 10, where τ_V is the optical depth at 0.55 μm. The calculations are presented for wavelengths 0.4000, 0.6563, and 1.00 μm and correspond to the $\theta = 90°$. Figures 4 and 5 show similar results for $\theta = 0°$ and $\theta = 45°$, respectively. The assumed properties for the grains are given in Table 1. The source velocity in units of v_0 has been taken as $v_s = -20$; taking $v_0 \approx 5 - 10$ km s^{-1}. This value of v_s corresponds to velocities of the order of those observed. In all the figures, profiles are normalized to the peak flux. For comparison, a gaussian line profile is shown as a dashed line. If the sign of the source velocity was changed

to positive, profiles would be similar to those shown in Figures 3 to 5, but with $-v$ of the axis changed to $+v$.

Profiles shown in Figures 3 to 5 illustrate the comments presented at the beginning of this section. The higher the value of τ_V, the stronger are wings around the intrinsic line profile of the source, since in this case the number of scatterers is larger. The effects are more pronounced at shorter wavelengths, since the extinction and the albedo are higher. Comparison of the profiles between the two grain mixtures for $\tau_V = 10$ at $\lambda = 1$ μm clearly shows this effect. The higher extinction and albedo in the case $a = 0.2$ μm results in stronger wings as compared to the SIM. In the case $\theta = 90°$, profiles are symmetric, while those at $\theta = 45°$ are not, as expected from the discussion above.

The effects of the asymmetry factor can best be seen comparing the series for different wavelengths at $\tau_V = 10$ and $a = 0.2$ μm (Figures 3b, 4b, and 5b), since in this case both the extinction and
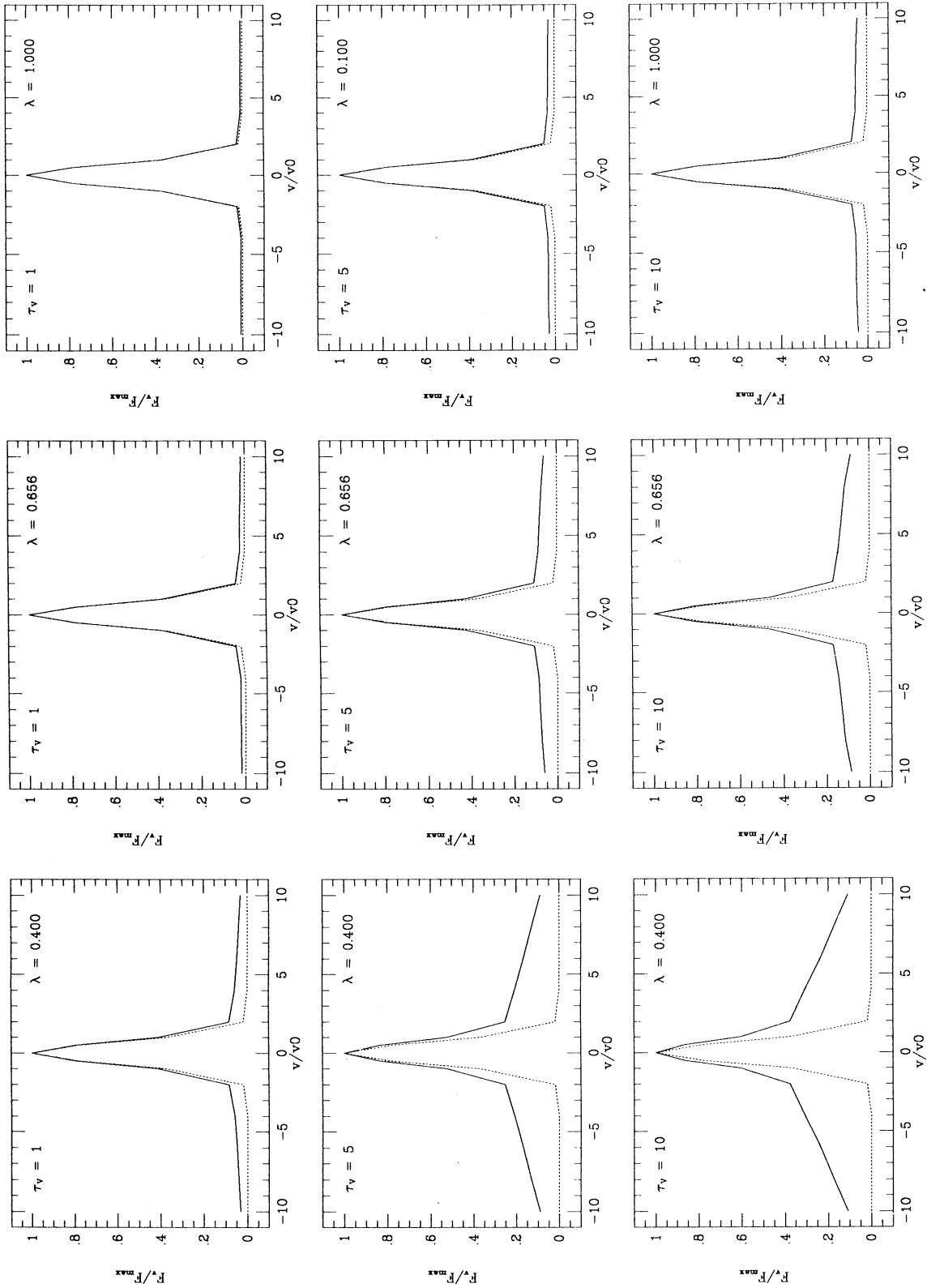
Fig. 3. (a) Line profiles for the standard interstellar mixture (SIM) and $\theta = 90°$. Profiles are shown for $\lambda = 0.4$, 0.6563, and 1.0 μm (left to right), and for $\tau_V = 1$, 5, and 10 (top to bottom). Profiles are normalized to the peak value. The source velocity is $v_s/v_0 = -20$. A gaussian profile with width equal unity is shown in dashed lines for comparison.
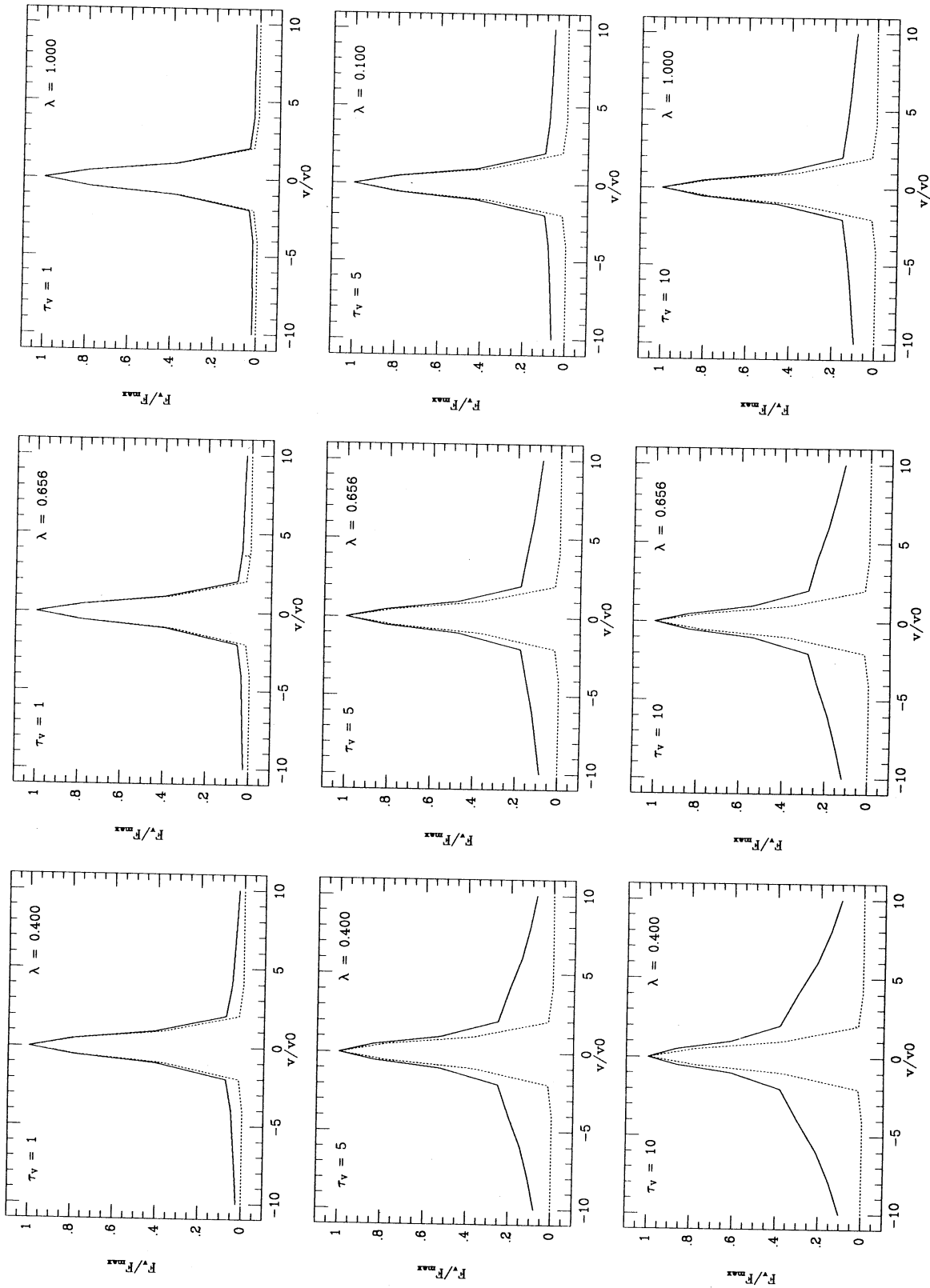
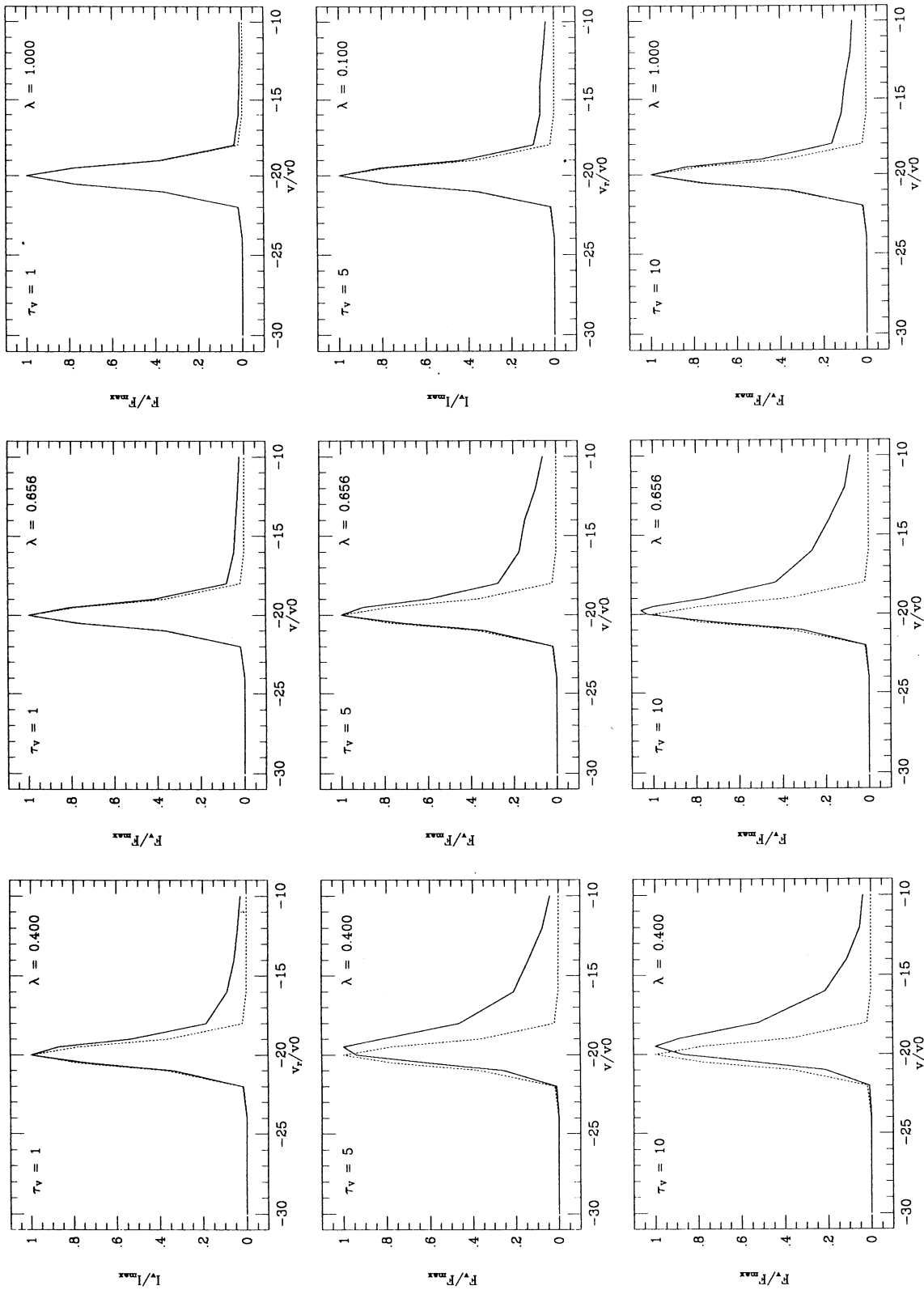Fig. 3b. Same as Figure 2a for grains with size $a = 0.2~\mu m$.
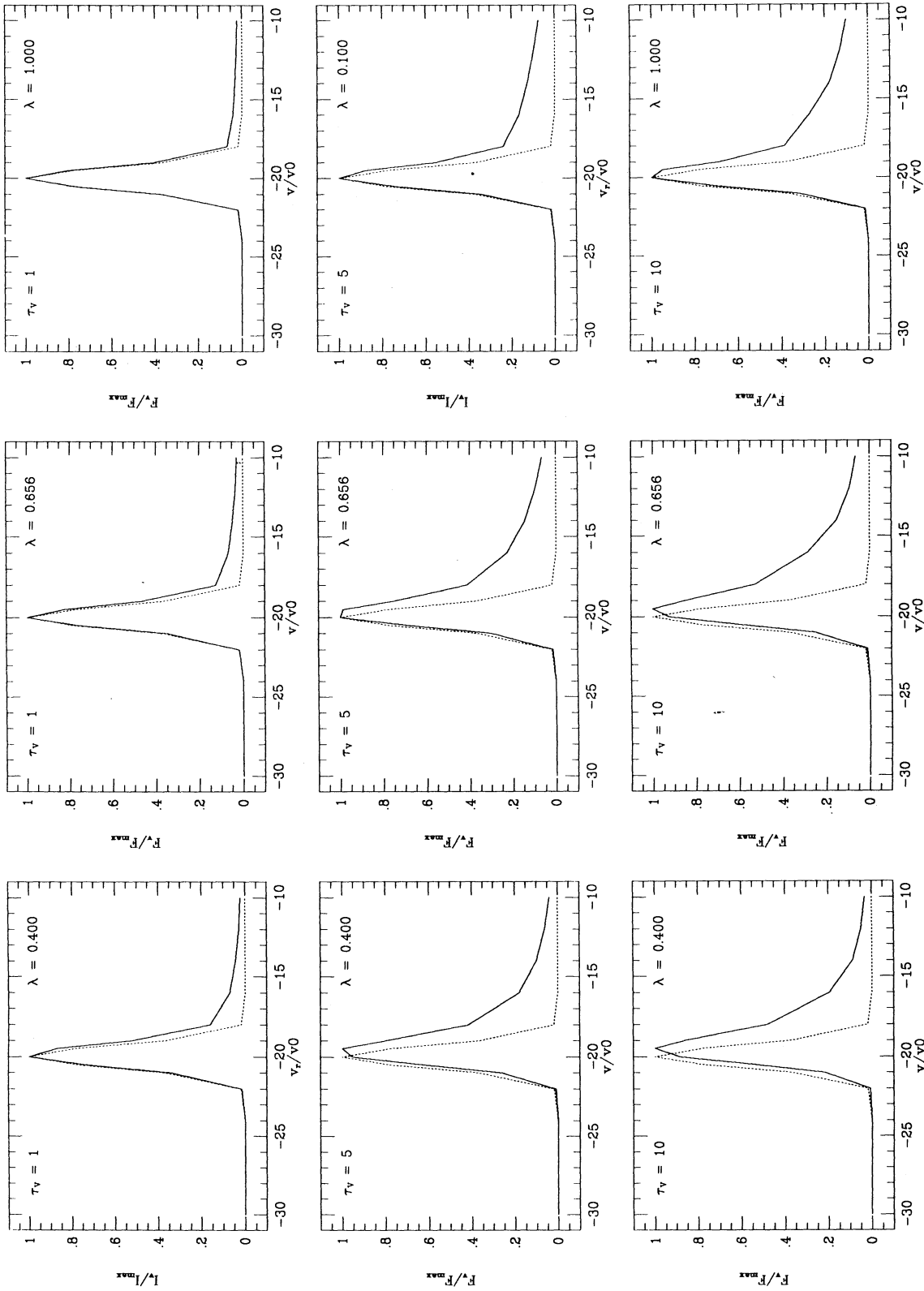
Fig. 4a. Same as Figure 3a for $\theta = 0°$.

Fig. 4b. Same as Figure 3a for $\theta = 0°$.

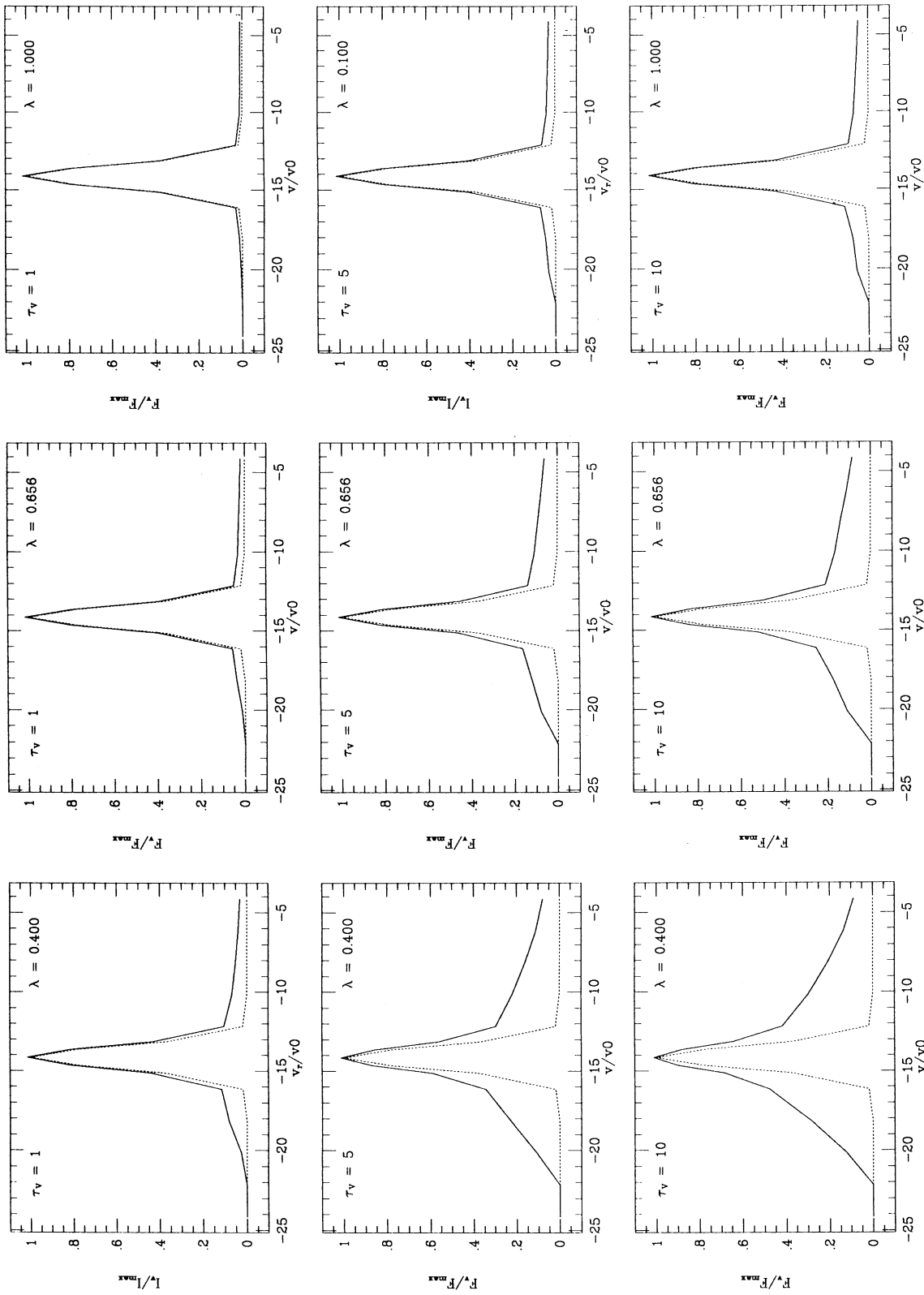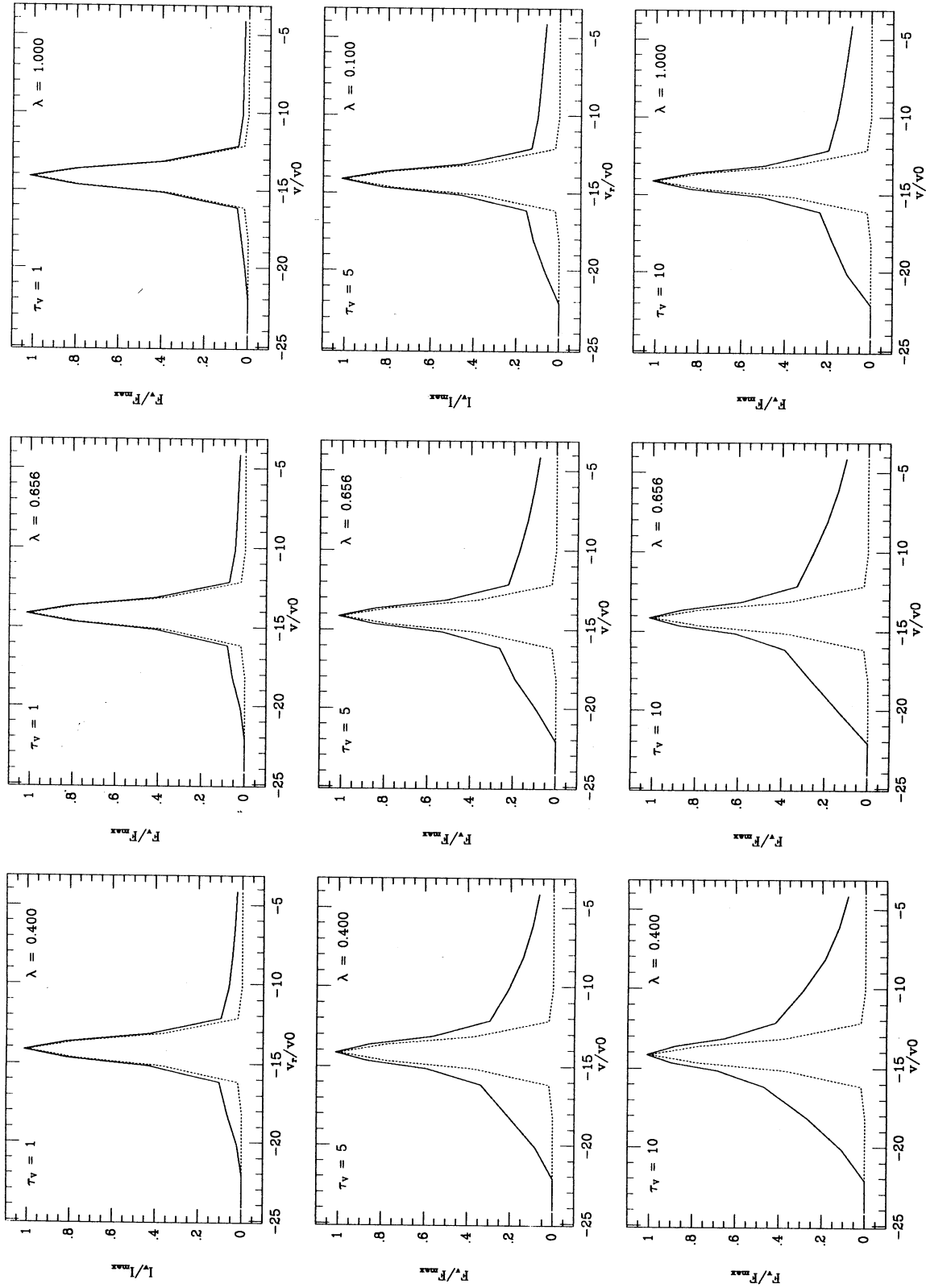Fig. 5a. Same as Figure 3a for $\theta = 45°$.

CALVET ET AL

Fig. 5b. Same as Figure 3a for $\theta = 45°$.

TABLE 1

ASSUMED GRAIN PROPERTIES

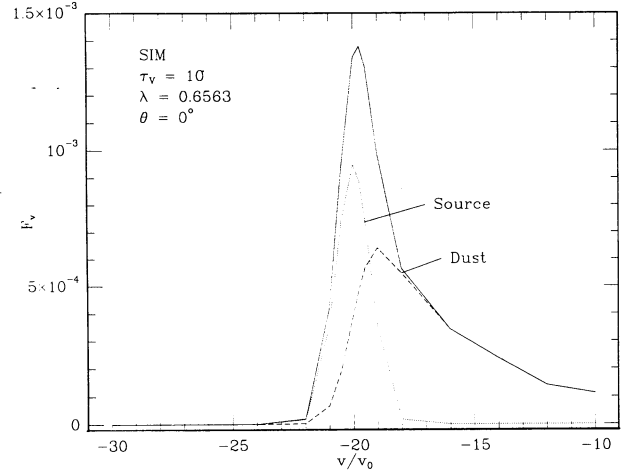| λ (μm)	0.4000	0.4861	0.6563	1.0000
SIM				
$\bar{a}_\lambda$	0.67	0.63	0.55	0.42
g_λ	0.63	0.55	0.44	0.24
$a = 0.2\mu$m				
$\bar{a}_\lambda$	0.757	0.758	0.744	0.703
g_λ	0.675	0.658	0.554	0.383

Fig. 6. Components of the line profile for the case τ_V = 10 and λ = 0.663 μm, SIM. The dust component introduces a shift of the resultant line profile relative to the source line profile.

the albedo are approximately similar at all wavelengths, while the phase function decreases as the wavelength increases (see Table 1). As λ decreases and g increases, there is more flux at velocities around $v_s \cos\theta$, due to the increased focusing action of the phase function.

An important effect shown in Figure 5 is that, at large τ_V and g, the center of the line shifts towards smaller absolute velocities, for the case $\theta = 0°$. This effect is due to the increasing importance of the dust contribution relative to that of the source, as can be seen in Figure 6, for the case $\tau_v = 10$ at $\lambda = 0.6563$ μm. Figure 6 shows the (extinguished) source emission, the dust emission, and the resultant total profile.

To understand this effect physically, we have developed an analytical model for the case $\theta = 0$, that is, v_s along the line of sight pointing towards the observer. Consider spherical coordinates. The observed line flux at velocity v can be written as

$$F_v = (1/d)^2 \int_0^{r_{max}} \int_0^\pi \eta_v e^{-\tau(z)} 2\pi r^2 \sin\Theta d\Theta dr , \quad (12)$$

where $z = z(r, \Theta)$, and $\tau(z) = \int_z^{z_{max}} \chi dz$, with $z_{max} = (r_{max}^2 - r^2 \sin^2\Theta)^{1/2}$. From equations (4) and (5), the emissivity is given by

$$\eta_v = (\sigma_v/4)\Phi(\Theta)(r_0/d)^2 I_0 e^{-\tau_r(r)} \times$$
$$\times e^{-[(v-v_s \cos\Theta)/v_0]^2} ; \quad (13)$$

and then,

$$F_v = (\sigma_v/2d^2)\pi r_0^2 I_0 \int_0^\pi \Phi(\Theta) \times$$
$$\times e^{-[(v-v_s \cos\Theta)/v_0]^2} \sin\Theta A(\Theta) d\Theta , \quad (14)$$

where

$$A(\Theta) = \int_{r_0}^{r_{max}} e^{-[\tau_r(r)+\tau(z)]} dr . \quad (15)$$

The term in brackets in equation (15) represents the total optical depth of a photon that is emitted at an angle Θ and is scattered at a distance r from the source. For a spherical, homogeneous cloud of radius r_{max}, this is given by

$$\tau_T = \tau_r(r) + \tau(z) = \chi[r(1 - \cos\Theta) +$$
$$+ (r_{max}^2 - r^2 \sin^2\Theta)^{1/2} - r_0] . \quad (16)$$

For the hemisphere $\Theta = 0$ to $\Theta = \pi/2$, the total optical depth is nearly constant (independent of Θ), provided that $r_{max} >> r_0$, with a value

$$\tau_T \approx \chi r_{max} . \quad (17)$$

Dust particles in this hemisphere will scatter photons with velocities in the range $(-v_s, 0)$. Therefore, for this velocity range,

$$A(\Theta) \approx r_{max} e^{-\chi r_{max}} ; \quad (18)$$

and then

$$F_v \approx (\sigma_v/2d^2)\pi r_0^2 I_0 r_{max} e^{-\chi r_{max}} P(v) , \quad (19)$$

where

$$P(v) = \int_{-1}^{1} \Phi(\mu) e^{-[(v-v_s\mu)/v_0]^2} d\mu , \qquad (20)$$

and $\mu = \cos\Theta$. Under these approximations, $P(v)$ is the function that determines the profile of the dust emission.

We may consider two limiting cases:

(i) $v_s = 0$, for which

$$P(v) = 2e^{-(v/v_s)^2} , \qquad (21)$$

which represents a gaussian profile centered at zero velocity, and

(ii) $v_0 << v_s$, for which, if $\Phi(\mu)$ does not change significantly within the width ($\Delta\mu = 2v_0/ \mid v_s \mid$) of the gaussian function in the integrand of equation (20),

$$P(v) \approx (\sqrt{\pi}/2)\Phi(\mu^*) \int_{-1}^{1} e^{-[(v-v_s\mu)/v_0]^2} d\mu ; \qquad (22)$$

where $\mu^* = v/v_s$ for $\mid v \mid < \mid v_s \mid$, and $\mu^* = 1$ for $\mid v \mid > \mid v_s \mid$, so

$$P(v) \approx (\sqrt{\pi}/2)\Phi(\mu^*)(v_0/v_s) \times$$

$$\times [erf(\frac{v_s + v}{v_0}) + erf(\frac{v_s - v}{v_0})]. \qquad (23)$$

If $\mu^* = v/v_s << 1$, the term in square brackets in equation (23) is $\approx$ constant $= 2$, that is, the integral in equation (22) behaves essentially as a δ-function with limits $-\infty$ and ∞. The velocity dependence of the line profile is determined basically by $\Phi(\mu^* = v/v_s)$; if $g << 1$, $\Phi \approx 1$, and the profile is nearly constant. As g increases and scattering becomes more anisotropic, the line profile becomes more
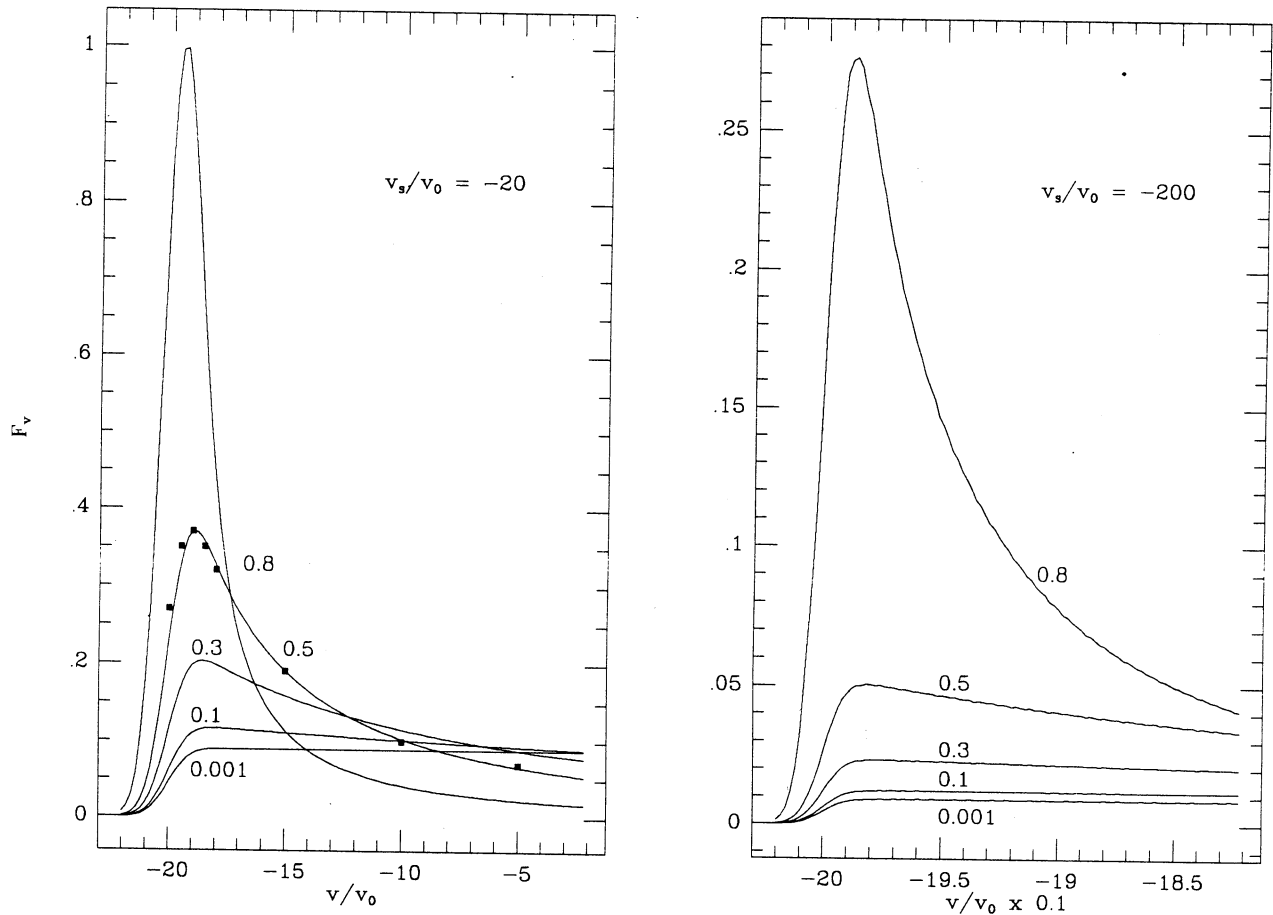

Fig. 7. Dust emission calculated from equation (20), shown for two values of v_s/v_0 and several values of the asymmetry parameter g. Values calculated with equation (23) are shown as filled squares for the case $v_s/v_0 = -20$ and $g = 0.5$. Curves are labeled by the value of g.

dependent on v. On the other hand, for μ^* closer to 1, the effects of the angle-cutoff ($\mu \leq \mu^*$) in the limits of the integral in equation (22) become important and the term in brackets becomes less than 2. This effect is less noticeable as v_0 decreases and the gaussian is narrower. For a large value of g, the dust emission has a maximum displaced from the source velocity, because of the cut-off at $v \approx v_s$. In Figure 7 we show the dust line profiles obtained by numerical integration of equation (20) for $v_0/v_s = -20$ and $v_0/v_s = -200$, and several values of g. These profiles illustrate the considerations made above. We also show in Figure 7 the profile given by equation (23) for $g = 0.5$. We can see that, in this case, the agreement is satisfactory.

The assumption used in deriving equations (22) and (23), namely, that $\Phi(\mu)$ does not change significantly within the width of the gaussian function in the integrand of equation (20), is valid if $v_0 <<| v_s |$ and g is not near unity. In particular, for isotropic scattering ($g = 0$, $\Phi(\mu) = 1$), equation (23) becomes exact. This approximation breaks down as $g \to 1$. This is due to the fact that $\Phi(\mu)$ becomes steeper as $g \to 1$ and cannot be considered constant in equation (20). We can quantify this statement by considering the relative change of $\Phi(\mu)$ around μ^* within the width $\Delta\mu = 2v_0/ | v_s |$, given by

$$\psi = \frac{1}{\Phi(\mu^*)} \left(\frac{d\Phi}{d\mu^*} \right)_{\mu^*} \Delta\mu^* \ . \tag{24}$$

From equation (6), this equation can be written as

$$\psi = \frac{6g}{(1 + g^2 - 2g\mu^*)} \frac{v_0}{| v_s |} \ , \tag{25}$$

which has a maximum value for $\mu^* = 1$,

$$\psi_m = \frac{6g}{(1 - g)} \frac{v_0}{| v_s |} \ . \tag{26}$$

Then, we expect equation (23) to be valid for $\psi_m << 1$ ($g \to 0$ or $v_0/ | v_s | \to 0$), and to break down for $\psi_m \approx 1$ ($g \to 1$). In this latter case, we can improve our approximation by expanding $\Phi(\mu)$ around μ^*. For instance, expanding at first order

$$\Phi(\mu) \approx \Phi(\mu^*) + \left(\frac{d\Phi}{d\mu^*} \right)_{\mu^*} (\mu - \mu^*) \ , \tag{27}$$

equation (20) becomes,

$$P(v) \approx (\sqrt{\pi}/2)\Phi(\mu^*)(v_0/v_s) \times$$
$$\times \left[erf\left(\frac{v_s + v}{v_0} \right) + erf\left(\frac{v_s - v}{v_0} \right) \right]$$
$$-(3/2)\frac{6g}{(1 + g^2 - 2g\mu^*)}\Phi(\mu^*)(v_0/v_s)^2 \times$$
$$\times \left[e^{-\left(\frac{v_s+v}{v_0} \right)^2} + e^{-\left(\frac{v_s-v}{v_0} \right)^2} \right] \ . \tag{28}$$

Better approximations can be obtained by considering higher orders in the expansion of $\Phi(\mu)$.

b) Reddening Determination

Although no determination of reddening has been made directly on any jet, it is usually assumed that the extinction is similar to that found towards HH objects. In turn, this extinction has been determined using the ratio of hydrogen lines or using the ratio of optically thin forbidden lines arising from the same upper level. These determinations usually assume that the extinction law is that of the standard interstellar mixture and moreover that only *attenuation* is present, without considering the effects of scattering. The latter effect, however, can distort the determination of the extinction of the region, with the consequent complication for comparison with theoretical models. We can use our calculations to estimate the error that would be made if only attenuation is taken into account. To do this, we calculate the ratio $(F_{\lambda_1}/F_{\lambda_1}^s)/(F_{\lambda_2}/F_{\lambda_2}^s)$ and the apparent optical depth τ_V^a by equating this ratio to exp $[-(\tau_{\lambda_1}/\tau_V - \tau_{\lambda_2}/\tau_V)\tau_V^a]$. In Table 2 and in Figure 8 we show the apparent optical depth assuming that only attenuation is present, τ_V^a, versus the true optical depth, τ_V, for the standard interstellar mixture and for $a = 0.2$ μm. The apparent optical depth has been calculated using two sets of wavelengths: (a) for 0.4 and 1 μm, which is meant to simulate the reddening determination using the [S II] lines at 0.4068 and 1.0287 μm, τ_V ([S II]), and (b) for Hα/Hβ, τ_V (H), (only τ_V ([S II]) is shown in Figure 8). Comparison between the true and ap-

TABLE 2

TRUE AND APPARENT OPTICAL DEPTH

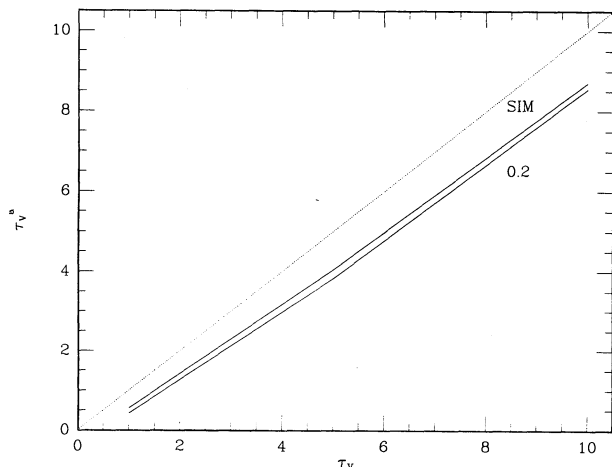| τ_V	τ_V^a ([S II])	τ_V^a (H)	τ_V	τ_V^a ([S II])	τ_V^a (H)
	SIM			$a = 0.2\mu$m	
1	0.55	0.54	1	0.42	0.35
5	3.96	4.00	5	3.83	3.65
10	8.71	8.79	10	8.56	8.19

Fig. 8. Apparent optical depth versus actual optical depth. Results are shown for the standard interstellar mixture and for a grain size $a = 0.2$ μm.

parent optical depths indicates that dust acts as an additional source of photons to the source proper, by scattering source photons towards the observer that would be lost if dust were not present. The system, source plus dust, is then intrinsically brighter than the source plus absorbing dust alone and the apparent optical depth is lower than the true one.

Apparent optical depth determined for different sets of indicators gives different results, as shown in Table 2. The differences are more significant in the case of large grains than for the SIM, although in both cases they may be within the observational errors.

In general, the optical depth determined by assuming only attenuation is lower than the actual optical depth in the region. Figure 8 can be used to get an estimate of the difference between the apparent and the actual optical depth. Different reddening indicators may give different values for the (apparent) optical depth, because the amount of scattered light at given wavelengths depends on the particular dust characteristics at that wavelength.

IV. DISCUSSION

a) Effect of Multiple Scattering

In the previous section, we have shown line profiles for the case in which light from a moving source is scattered by a static dusty medium surrounding it. We have applied the treatment even to the case of large optical depths, which may be questionable given the single-scattering assumption. In any event, extended wings are always produced, because their existence depends only on the relative velocity between the source and the first scatterer. For any photon, subsequent scatterings do not change the velocity position within the line profile.

Since we have assumed that each photon is scattered only once, the emissivity at each point in the medium is determined only by the energy scattered from the central source. In the case of multiple scattering, the emissivity at a given position in the profile would have an additional contribution from photons scattered by other particles in the medium towards that point. On the other hand, when we integrate along each line of sight, we calculate the optical depth using the total extinction, that is, absorption plus scattering. We are therefore naturally including the case of multiple scattering in the calculation of the emergent flux. Hence, in the integration along each line of sight, we calculate properly the amount of energy taken out of the line, but do not include all the photons that are scattered back into the line of sight. We then expect that the amount of energy coming out at a given velocity will be *underestimated* by our treatment for the case of large optical depths. The line wings calculated by us are then *lower limits* to the true wings. The underestimation will increase as the optical depth of the medium increases. Monte Carlo calculations with multiple scattering but correspondingly larger τ_V, could show to what extent the profiles are the same as those calculated here with single scattering.

b) Comparison with Observed Profiles

The comparison of theoretical line profiles with observations can give an indication of the strength and the direction of the source velocity relative to the line of sight. For instance, the [S II]$\lambda\lambda$ 6717, 6731 line profiles in knots E+F of the jet associated with HH 34 (Bührke et al. 1988), located at the beginning of the bright region in the jet, have a wing that extend towards velocities less negative than that of the peak. The position-velocity diagram in [S II] λ 6716 shows that the position of the peak shifts towards a less negative velocity and wings develop in both sides of the peak further down along the jet. Comparison with line profiles in Figures 4 to 6 suggests that when the jet is coming out of the cloud, it is moving at a small angle to the line of sight, producing profiles similar to those in Figure 5. Further down it bends towards larger angles, and the profiles are better described by those in Figure 5. In this model, the observed velocity of the peak at knots E+F would be indicative of the source velocity, while that at knots G-K would be $v_s \cos\theta$. If we assume that bending does not change the source velocity, then a bending of $\approx 28°$ would be required to explain the observations. Meaburn and Dyson (1987) show line profiles for the [S II]$\lambda\lambda$ 6717, 6731 and Hα lines in the jet HH 47B. In this case, comparison with theoretical profiles suggests that we are seeing the jet at inclinations $\theta \approx 45°$, since the wings are asymmetric (in Hα), with the blue wing falling more sharply than the red wing.

Comparison with theoretical line profiles can also give an indication of the optical depth in the medium and of the size of the source. In both cases discussed above, namely, the jet associated with HH 34 (knots E+F) and HH 47B, it is noticeable that the [S II]$\lambda\lambda$ 6717, 6731 profiles and the Hα profile are different. In the first case, while the [S II] lines have a red extended wing superimposed on a well defined approximately gaussian peak, the Hα profile has a smaller contrast between the peak and the red excess, and moreover the peak is shifted towards velocities redder than those of the peak of the [S II] lines (Bührke *et al.* 1988). In the case of HH 47B, the Hα profile shows strong wings, while these are much weaker in the [S II] lines (Meaburn and Dyson 1987). The difference in both cases can be understood in this model as indicative of a larger optical depth towards the region where the Hα line forms than towards the region where the [S II] lines form. The "fat" profile in Hα in the HH 34 jet, where the peak is shifted relative to the source velocity (as given by the peak velocity of the [S II] lines) can be understood in terms of optical depths $\tau_V > 5$, considering that the profiles shown in Figure 5 have only lower limits for the dust scattering component. In contrast, optical depths $\tau_V \approx 1$ could explain the [S II] wings for this object. A similar explanation could be applied to HH 47B, where $\tau_V \approx 5$ could explain the Hα profile, while $\tau_V \leq 1$ could be appropriate for the [S II] lines. The difference in optical depth could be due to a different size of the emitting region, with the region emitting Hα being 4 to 5 times smaller than that emitting the [S II] lines.

The detailed calculated profiles do not agree with the observed ones. In particular, the calculated wings are smooth and do not reproduce the smaller peaks interpreted as the low velocity component. However, inspection of the direct images of the jets discussed indicate that the spatial distribution of these smaller peaks and even their velocity vary. In our discussion of dust scattering we have assumed that the medium was uniform. If it is not, then one would expect a wing with an overall shape as that calculated, but with excesses or deficits of emission depending on the density of the regions where the flux at the given velocity would be coming from. In addition, it is likely that including multiple scattering in the calculation of the emissivity will improve the comparison in future

studies. Nonetheless, the results presented here are encouraging enough to justify these future studies.

V. SUMMARY

The main results of this work are:

1) We have found that the result of scattering by dust particles in the stationary medium surrounding the moving gas that forms the jet, is to produce extended wings in the line profiles. The strength and extent of these wings depend only on the dust properties and on the optical depth of the medium.

2) With the scattering hypothesis, the overall shape of the extended wings seen in the [S II] $\lambda\lambda$ 6716, 6730 and in the Hα lines, in observed jets, can be explained. Comparison with theoretical line profiles can give estimates of the inclination of the jet to the line of sight, of the jet velocity, and the optical depth towards the source.

3) In regions where there is a large amount of dust, reddening determinations which include only the effect of attenuation are not correct. Scattering by dust acts as an additional source of photons, so that lines appear brighter and the derived optical depths smaller than they really are. The difference between the true and apparent optical depth depends on the dust properties of the region.

REFERENCES

Bruzual A., G., Magris C., G., & Calvet, N. 1988, ApJ, 333, 673

Bührke, T., Mundt, R., & Ray, T.P. 1988, A&A, 200, 99

Cantó, J.T., Raga, A.C., & Binette, L. 1989, RevMexAA, 17, 65

Cantó, J.T., & Raga, A.C. 1991, ApJ, 372. 646

Draine, B.T. 1987, Princeton Observatory Preprint No. 213

Draine, B.T., & Lee, H.M. 1984, ApJ, 285, 89

Feldman, H.A., & Raga, A.C. 1991, preprint

Henyey, L.G., & Greenstein, J.L. 1941, ApJ, 93, 70

Lillie, C.F., & Witt, A.N. 1976, ApJ, 280, 64

Mathis, J.S. 1983, ApJ, 267, 119

Mathis, J.S., Rumpl, W., & Nordsieck, K.H. 1977, ApJ, 217. 425

Meaburn, J., & Dyson, J.E. 1987, MNRAS, 225, 863

Morgan, D.H., Nandy, K., & Thompson, G.I. 1976, MNRAS, 177, 531

Mundt, R. 1988, in NATO ASI, Formation and Evolution of Low Mass Stars, eds. A.K. Dupree and M.T.V.T. Lago, (Dordrecht: Kluwer), p. 150

Noriega-Crespo, A., Calvet, N., & Böhm, K.-H. 1991, ApJ, in press

Luc Binette: Canadian Institute for Theoretical Astrophysics, 60 St. George Street, Toronto, Ontario M5S 1A1, Canada.

Nuria Calvet: Centro de Investigaciones de Astronomia, CIDA, Apartado Postal 264, Mérida 5101-A, Venezuela.

Jorge Cantó: Instituto de Astronomía, UNAM, Apartado Postal 70-264, 04510 México D.F., México.

Alejandro C. Raga: School of Mathematics, The University, Leeds LS2 9JT, U.K.